Electronic Supplementary Material (ESI) for ChemComm.

Supplementary Information

The Photoluminescence Spectral Profiles of Water-Soluble Aggregates of PbS Quantum Dots Assembled through Reversible Metal Coordination

*Chen Wang, Mohamad Saeed Kodaimati, George C. Schatz, and Emily A. Weiss**

Department of Chemistry, Northwestern University, 2145 Sheridan Rd., Evanston, IL 60208-3113

*corresponding author. Email: e-weiss@northwestern.edu

Table of Contents

1. Synthesis of PbS Quantum Dots.

We synthesized oleate-capped PbS quantum dots using a protocol adapted from Hines, *et al.*.[1] We dissolved 0.36 g lead oxide (PbO, Sigma-Aldrich, 99.999%) in 20 ml solution of 1-octadecene (ODE, Sigma-Aldrich, 90%) and oleic acid (OA, Sigma-Aldrich, 90%) in a 50 ml three-neck flask at 150 °C under N_2 atmosphere. The temperature of the solution was maintained at 150 °C for 30 min before being cooled to 110 °C. We then pulled vacuum (<0.1 torr) on the solution for 15 min to remove water, and returned it to N_2 atmosphere. We used bis(trimethylsilyl)sulfide (TMS, Sigma-Aldrich) as the sulfur precursor. The precursor solution was prepared by dissolving 0.17 ml of TMS in 8 ml ODE, and purged with dry N_2 for at least 1 hour at ambient temperature. After quickly injecting the sulfur precursor into the solution of lead oleate, we let the mixture react for 10 min at 100 °C. We added 100 mL methanol to the reaction mixture to wash the PbS QDs. We centrifuged the mixture at 3500 rpm for 20 min. After removing the supernatant, the QDs were precipitated again by adding 50 mL acetone and centrifuging at 3500 rpm for 20 min. We redispersed the resulting pellet with a small amount of hexanes, added 50 mL acetone, centrifuged at 3500 rpm for 20 min a third time, removed the supernatant, dried the QD pellets under N_2 flow, and dispersed the QDs in chloroform. The size of the QDs was controlled by the concentration of OA used in synthesis. For the donor QDs (DQD, first excitonic absorption peak at 900 nm, radius = 1.6 nm), 1.05 ml of OA and 18.95 mL ODE were used, and for acceptor QDs (AQD, first excitonic absorption peak at 1040 nm, radius = 1.8 nm), 3.5 ml OA and 16.5 ml ODE were used.

2. Ligand Exchange to Glutathione (GSH).

We exchanged the native oleate ligands of the QDs for GSH through a phase transfer procedure. The as-synthesized oleate-capped QD solution was diluted with $CHCl_3$ to ~10 μM, and mixed with the same volume of an aqueous solution of GSH with a concentration of 1 mM and a pH of 7. We vortexed the mixture for 30 min, and separated the organic and aqueous layers by centrifugation at 3500 rpm for 5 min. The procedure was repeated for four times and the aqueous solution of GSH-capped QD was collected and purged with N_2 for one hour before filtering with a 0.22-μm syringe filter. The first excitonic absorption band peaked at 932 nm for the GSH-capped DQDs, and peaked at 1056 nm for the GSH-capped AQDs.

3. Dynamic Light Scattering.

We measured the hydrodynamic diameters of the dispersed QDs and the aggregates with a dynamic light scattering analyzer (Malvern, Zetasizer Nano). The samples were contained in a 1-

cm path-length cuvette and illuminated with 633-nm He-Ne laser at 25 °C. The dispersed QDs have an average hydrodynamic diameter of 9 ± 2 nm, and the average particle size increases to 51 ± 12 nm after coupling with Zn^{2+} (**Figure S1A**). The average particle size upon assembly plateaued at concentrations of Zn^{2+} higher than 10 eq per QD (**Figure S1B**), whereas the PL spectra of the mixtures continued to change with increasing of Zn^{2+} even above this concentration. We interpret this result to mean that, at low concentrations of Zn^{2+}, the QDs formed loosely bound aggregates, and increasing the Zn^{2+} concentration decreased the average interparticle distance within these aggregates.

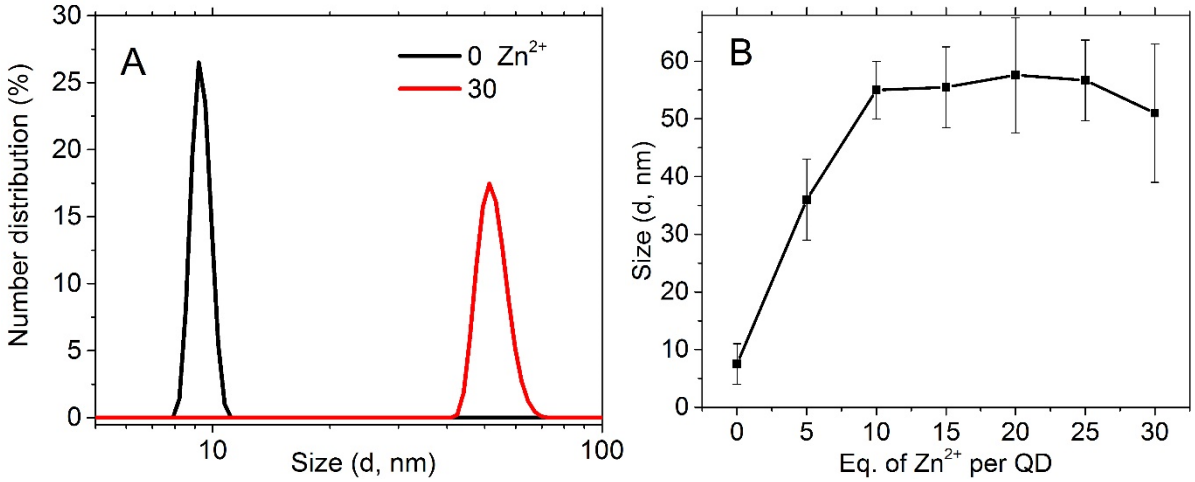

Figure S1. (A) DLS data for the dispersed mixture of DQDs and AQDs with molar-ratio of 3:1, and the same DQD/AQD mixture coupled with 30 eq. of $ZnCl_2$ at pH = 7. **(B)** The average particle size in the coupled DQD/AQD mixtures measured by DLS as a function of Zn^{2+} concentration.

4. Cryogenic Scanning Transmission Electron Microscopy (Cryo-STEM).

200-mesh lacey carbon Cu grids were glow discharged in a Pelco Easiglow glow-discharger for 30 seconds and loaded into a Vitrobot Mark III cryo plunge-freezing instrument. 4 μL of each sample was pipetted onto the grid and blotted for 4 seconds with a 0.5 mm blot offset before plunging into liquid ethane. Plunge-frozen grids were carefully placed into a Gatan cryo-TEM holder, cooled down to -172 °C, and imaged in Hitachi HD-2300A field emission STEM at 200kV (55 μA of current) utilizing the bright field phase contrast imaging mode.

We measured the diameters of 56 QD clusters and fit the data with a Gaussian distribution to yield the average particles size of 35 ± 8 nm (**Figure S2**). The average center-to-center distance between QDs within the cluster was determined by fitting the results of 242 measurements with the Gaussian statistics, and yielded d = 4.8 ± 0.6 nm (**Figure S3**).

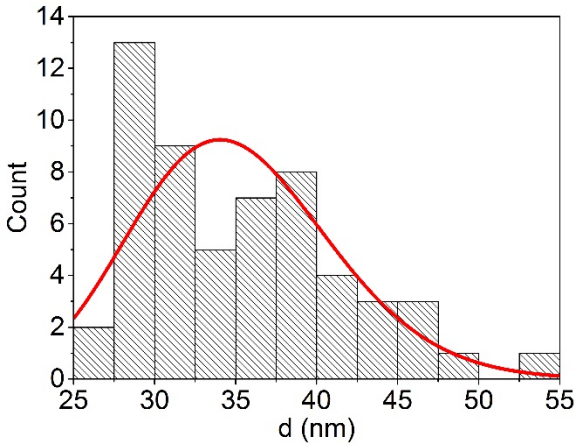

Figure S2. The distribution of diameters of QD assemblies, measured by cryo-STEM. The assemblies were formed from a DQD:AQD=3:1 mixture with 30 eq. of Zn^{2+} at pH=7. The sampling size is 56 and the bin size is 3 nm.

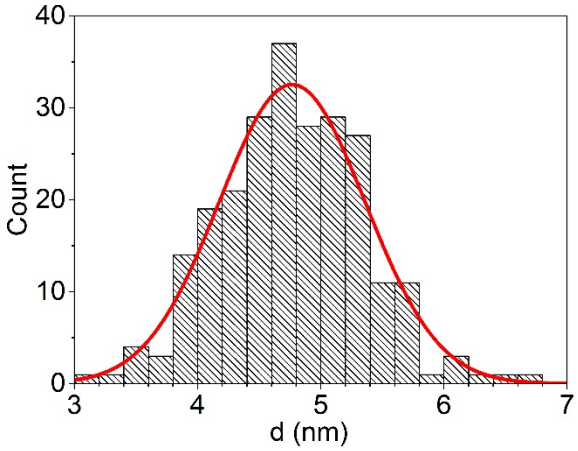

Figure S3. The distribution of the center-to-center interparticle distances within assemblies formed from a DQD:AQD=3:1 mixture with 30 eq. of Zn^{2+} at pH=7. The sampling size is 242 and the bin size is 0.2 nm.

5. Steady State Absorption and Photoluminescence Measurements.

We measured ground state absorption spectra of the samples with an Agilent Cary 5000 spectrometer. Samples were measured in a 1-cm quartz cuvette. The photoluminescence (PL) spectra were measured with a Horiba Fluorolog-3 spectrofluorometer using a right-angle geometry and a 2 mm/1cm dual-pathlength cuvette. The excitation beam was applied along the 1-cm path of the cuvette, and the excitation slit width was 5 nm. The sample emission was collected along the 2-mm path with a slit width of 2 nm. PL spectra were corrected for the absorption of the water between the 1000 – 1350 nm region.

The coupling of QDs upon adding Zn^{2+} was monitored with steady-state PL spectra for samples with different DQD:AQD ratios, with different coverages of GSH ligand, and under different pH

values (6.2 - 9.4). All QD mixtures composed of different DQD:AQD ratios show a >90% decrease of DQD PL at 1000 nm and increase of AQD PL at 1200 nm after adding 30 eq. Zn^{2+} at pH=7 (**Figure S4**). QDs with a lower surface coverage of GSH ligands require less Zn^{2+} (15 eq.) to achieve a similar degree of PL change as the sample shown in the main text (**Figure S5**). The aggregation of QDs with Zn^{2+} was also controlled by modifying the pH of the solutions before coupling (**Figures S6,S7**). When at pH ≤ 7, mixtures with DQD:AQD = 3:1 required 30 eq. Zn^{2+} to decrease the DQD PL to <10% of the original intensity. Further increasing the Zn^{2+} concentration did not change the final line-shape of the PL spectrum, but did slightly decrease the final PL intensity (**Figure S8**). At pH > 7, the amount of Zn^{2+} needed to achieve a given degree of QD aggregation (i.e., DQD quenching) increased with increasing pH. We attribute the pH dependence of QD aggregation to the formation of $Zn_x(OH)_y^{(2x-y)}$ complexes, which inhibits the interaction of Zn^{2+} with the GSH ligands. The PL QY of the coupled sample increased with the pH; we suspect this is due to the formation of $Zn_x(OH)_y^{(2x-y)}$ complexes which inhibits exchange of Zn^{2+} with Pb^{2+} on the QD surface. We observed that, after assembling the QDs using Zn^{2+}, further increasing the solution pH does not disaggregate the assemblies, **Figure S9**.

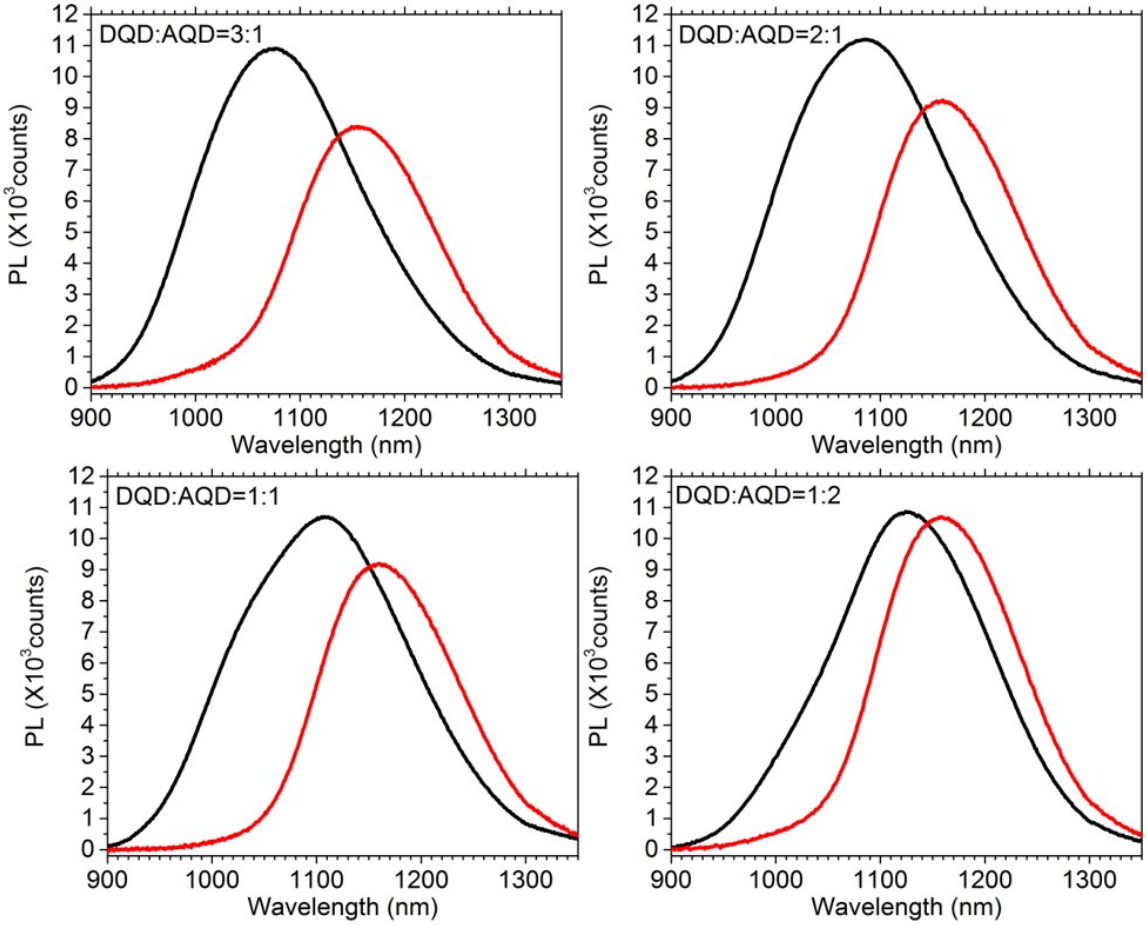

Figure S4. The steady-state PL spectra of the dispersed (black) mixtures with different DQD:AQD ratios and the same samples coupled with 30 eq. Zn^{2+} (red) at pH=7. The spectra are collected with 450 nm excitation.

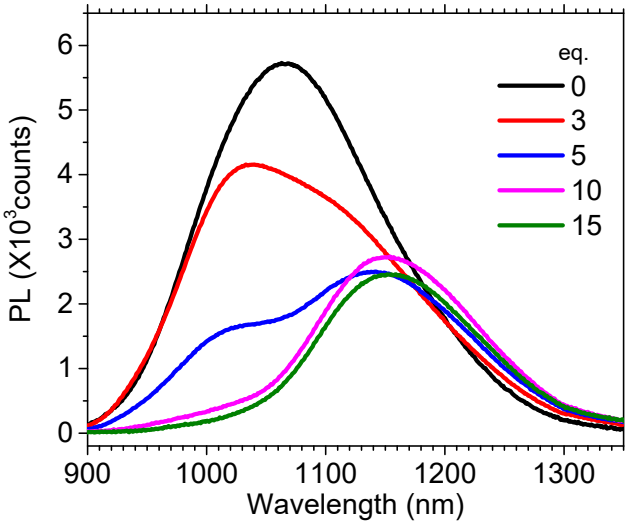

Figure S5. The evolution of steady-state PL spectra of the DQD:AQD = 3:1 samples when adding $ZnCl_2$ at pH=7. The QDs were collected from the second round of GSH exchange, and therefore had a lower GSH coverage compared to the sample shown in the main text.

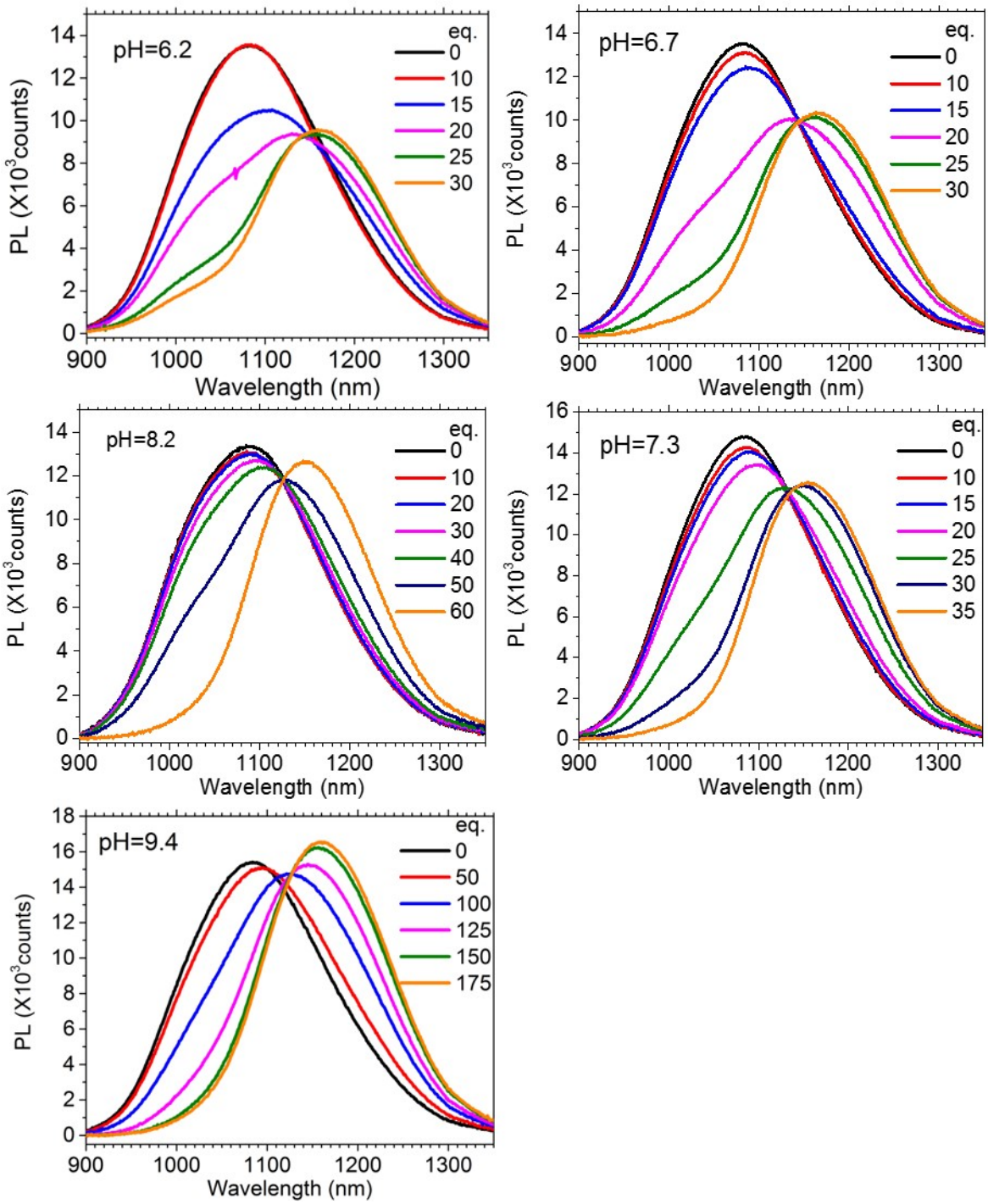

Figure S6. The evolution of steady-state PL spectra of the DQD:AQD = 3:1 samples when adding $ZnCl_2$ at different pH values. The spectra were collected with 450 nm excitation.

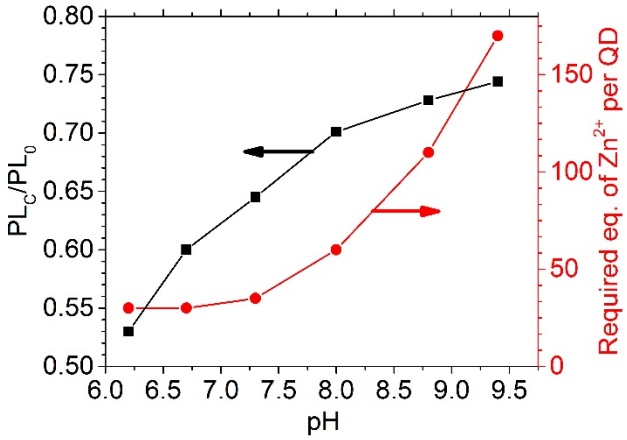

Figure S7. (*Red, right axis*): The amount of Zn^{2+} necessary to reach the maximum yield of FRET (where the PL of the DQDs at 1000 nm is quenched by ≥90% and the PL intensity of the AQDs saturates), as a function of initial solution pH for mixtures with DQD:AQD = 3:1. The total concentration of QDs in the sample is 1 μM. (*Black, left axis*): The integrated PL intensity ratios of the same set of DQD/AQD samples before (PL_0) and after (PL_C) coupling with Zn^{2+} as a function of initial solution pH. As the initial pH increases the fraction of total PL of the sample preserved upon assembly increases.

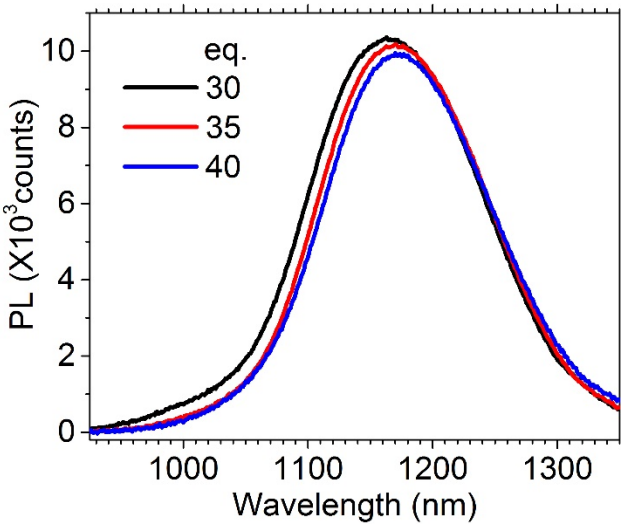

Figure S8. Steady-state PL spectral evolution for DQD:AQD=3:1 sample at pH=7 with Zn^{2+} concentration higher than 30 eq.

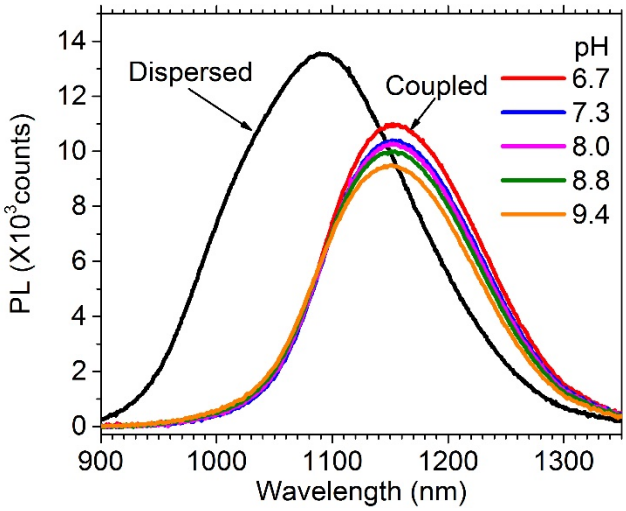

Figure S9. The evolution of steady-state PL spectra at different pH for a DQD:AQD = 3:1 mixture after coupling with 30 eq. $ZnCl_2$ at pH=7.

We also observed the aggregation of QDs within pure DQD-only and AQD-only samples by monitoring the change of their PL spectra upon the addition of Zn^{2+} (**Figure S10**). PL spectra of both DQDs and AQDs appear red-shifted (40 nm for DQD and 20 nm for AQD) after adding 30 eq. of Zn^{2+} while their absorption spectra remain the same. We attribute the redshift of the PL spectra to energy transfer from smaller QDs to the larger QDs within the QD aggregates. This observation agrees with that of the DQD-AQD mixtures, which have a bathochromically shifted AQD steady-state PL spectrum after coupling, **Figure S11**, bottom panel. The time-resolved PL kinetics confirm that the DQD and AQD-only samples undergo FRET, shown below. The PL intensity of the DQDs and AQDs decreases after coupling with Zn^{2+}. The DQDs undergo more dramatic quenching of PL (40%) as compared to the AQDs (15%).

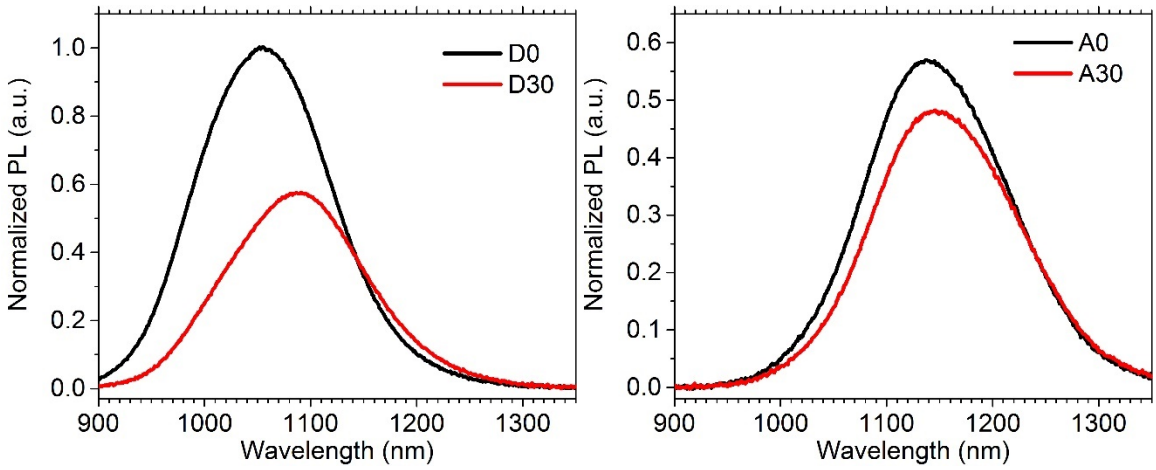

Figure S10. PL spectra of DQDs and AQDs upon the addition of 30 eq. Zn^{2+} at pH=7. The "D0" spectrum was normalized to its maximum and the other spectra were scaled by their respective peak intensities relative to D0 and by their respective absorbances at the excitation wavelength, 823 nm, relative to D0. We suspect the quenching of the PL shown in Figure S10 is due to a combination of Zn^{2+} reacting with the QD surface and FRET to non-emissive QDs within the ensemble.

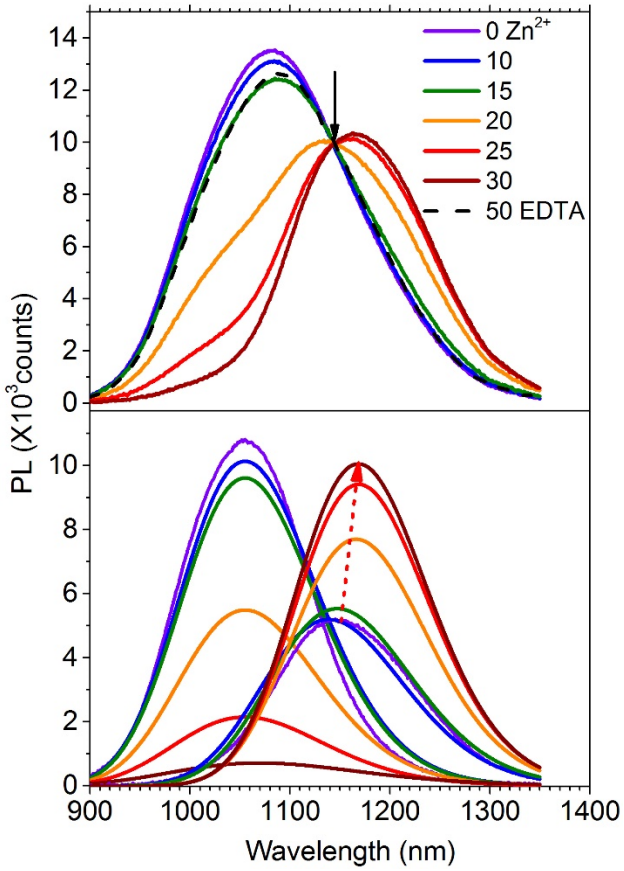

Figure S11. *Upper panel:* The evolution of steady-state photoluminescence spectra of the mixture of DQDs and AQDs with molar-ratio of 3:1 when adding different amounts of $ZnCl_2$ at pH 7. The arrow points to an isosbestic point. A spectrum of the same sample with 30 eq. of Zn^{2+} after adding 50 eq. of EDTA is plotted (black dashed line) to show the reversibility of the coupling. The spectra

are collected with 450 nm excitation, where the optical density of the DQD is 0.31, and that of the AQD is 0.13. *Lower panel:* Deconvolution of upper panel spectra with DQD and AQD PL to illustrate the decrease of DQD emission and the increase of AQD emission after coupling with different eq. of Zn^{2+}. The deconvolution was carried out by fitting the experimental spectra with two Gaussian bands with the DQD peak position fixed at that for pure DQDs at 1055 nm, while allowing the other parameters to float. The red dashed arrow indicates the growth and bathochromic shift of AQD PL with coupling.

6. DFT calculation for GSH-Zn-GSH complex.

Quantum chemical calculations were performed using the density functional theory (DFT) method with Nwchem 6.5 software[2]. Geometry optimization of the complex were carried out using the B3LYP functional with an effective core potential basis set for the Zn (LANL2DZ) and the 6-31+G** basis set for all other atoms. The final optimized geometry is in **Figure S12**. The through-space distance between the two sulfur atoms is 11.7 Å.

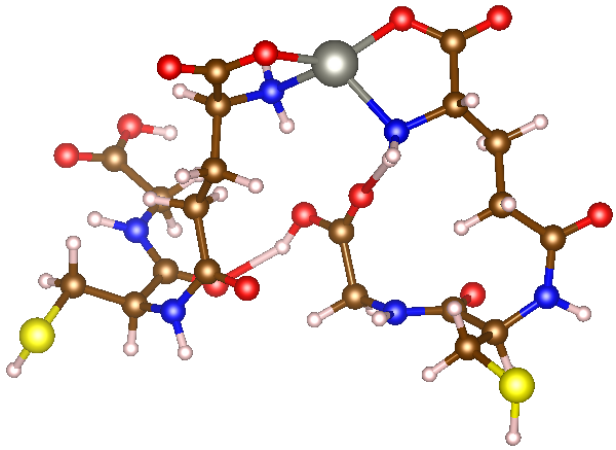

Figure S12. The DFT optimized molecular structure of a GSH-Zn-GSH complex.

7. Time-Resolved Photoluminescence Experiment (TR-PL).

We measured the dynamics of the photoluminescence of AQDs and DQDs with a home-built time-correlated single photon counting (TCSPC) setup. The samples were excited with 450 nm pulses from a diode laser (PicoQuant model no. LDH-P-C-450B) at a repetition rate of 100 KHz. We used a 900nm long- pass filter to block scattered photons from the pump. The samples with a total QD concentration of 1 μM were held in a 1-cm pathlength quartz cuvette. PL signals of the DQD and AQD samples were selected using a 1000-nm short pass filter and a 1200-nm long pass filter, respectively. The PL from the sample was focused onto a fiber optic and recorded by an InGaAs NIR detector to use as a trigger signal for photon counting. A timer-counter analyzer (Pendulum CNT91) was used to measure the delays between the trigger signals and the stop

(photon arrival) signals, which were synchronized with laser pulses. The results were collected as a histogram with a binning size of 200 ps by a home-written LabView program.

The original exciton lifetimes of uncoupled DQDs and AQDs are 1570 and 1100 ns, respectively (**Figure S13**).

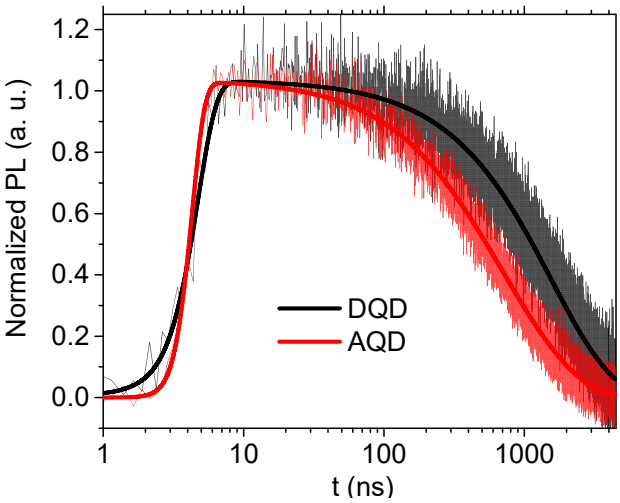

Figure S13. Time-resolved PL traces uncoupled DQDs at emission wavelengths of 900 - 1000 nm and AQDs at >1200 nm after 450 nm excitation. The kinetic traces are fit with single exponential decays.

8. Exponential fitting of the FRET kinetics in QD assemblies.

The PL kinetics of the coupled sample, which represent the EnT dynamics, were initially fitted with multiple exponential components (**Figure S14**). Kinetic traces between 900 and 1000 nm record the decay of the smallest DQDs kinetics. The DQD-only trace can be fit with three exponential decays. Two of them, with time constants of 16.4 and 97 ns, represent EnT from the smallest DQDs to larger ones. The component with the longest lifetime (710 ns) is assigned to the intrinsic exciton relaxation of coupled DQDs in the assemblies. Fitting the data for assemblies comprising both DQDs and AQDs yields two fast decay terms with time constants of approximately 11 and 40 ns. We therefore globally fit all the DQD kinetics by sharing time constants as listed in **Table S1**. For DQD/AQD coupled samples, the longest decay lifetime (τ_3 = 620 ns) is slightly smaller than the intrinsic exciton lifetime obtained from fitting the DQD-only data (τ = 710 ns), implying there might be another slow EnT process with a time constant of hundreds of nanoseconds.

We fit the kinetic traces recording at PL >1200 nm with one or two exponential growth terms and one exponential decay term, as shown in **Figure S14B** and **Table S2**. These kinetic traces

represent changes of exciton population in AQDs with the largest sizes. For AQD only data, we also observed a growth component due to EnT from AQDs with smaller sizes. The intrinsic lifetime of AQDs in the coupled assemblies is 677 ns. It is worthwhile to emphasize that the AQD TR-PL monitored at >1200 nm represents the acceptors with the smallest bandgap; the energy in these QDs does not have any available EnT pathways. The decrease of exciton lifetime from 1100 ns to 677 ns is purely due to the formation of surface trap states in the presence of Zn^{2+}. All fitting results for assemblies with different DAD:AQD ratios consist of a fast growth with time constants of 10~18 ns, and another slow growth with time constants ranging from 31 to 55 ns, which are similar to the two decay components observed for the DQD kinetics. The lifetimes of the decay components in the AQD kinetics of all DQD-AQD mixtures are longer than 677 ns, and increase with the fraction of QDs that are DQDs, suggesting the existence of an undistinguished slow EnT process.

We noticed that, with the increase of DQD population, the fractional amplitude of the faster component (τ_1 = 10.6 ns) in the DQD (900-1000 nm) kinetics decreases, while that of the τ_2 = 42 ns component increases, which can be understood as the decrease of the number of fast EnT pathways. However, the observation that the average EnT time constants for the AQD kinetics (>1200 nm) increase for assemblies consisting more DQDs is counter intuitive. Therefore, a more sophisticated kinetic model is necessary to understand the exciton migration in these QD assemblies.

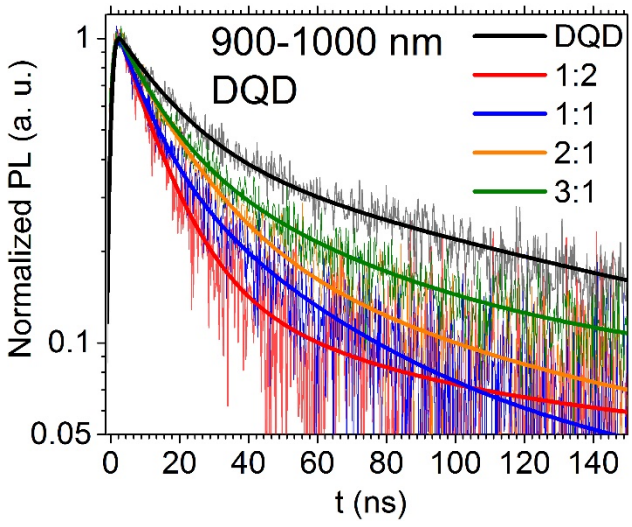

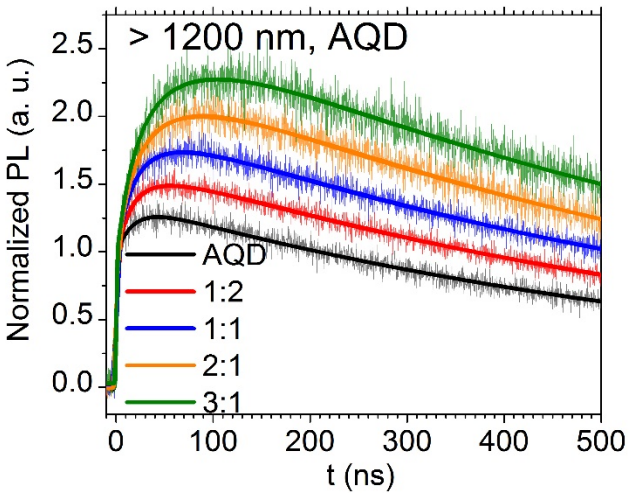

Figure S14. Time-resolved PL traces for samples of coupled QDs with different DQD:AQD ratios, monitored at emission wavelengths of 900 - 1000 nm (mostly DQD emission) and >1200 nm (mostly AQD emission) after 450 nm excitation. All samples have a total QD concentration of 1 μM and are coupled with 30 equiv. of Zn^{2+} at pH = 7. DQD (<1000 nm) kinetic traces are normalized to their peak maximum and AQD (>1200 nm) kinetic traces are normalized to their amplitudes after the instrument response (2.5 ns). The kinetic traces of DQD/AQD mixtures are globally fit with three exponential terms with shared time constants, while kinetic traces for DQD-only and AQD-only samples are fit separately with double-exponential. All fitting parameters are listed in **Tables S1** and **S2**.

Table S1 Global Multi-Exponential Fitting Parameters for the Dynamics of DQD PL within Coupled QD Assemblies.

DQD:AQD	OD_D/OD_A at 450 nm	τ_1 = 10.6 ± 0.3 ns[a] amp. EnT	τ_2= 42 ± 2 ns[a] amp. EnT	τ_{EnT} (ave.)[b] ns	τ_3= 620 ± 14 ns[a] amp. Intrinsic decay
1:2	0.14/0.33	0.83 ± 0.01	0.11 ± 0.01	11.6 ±0.3	0.06 ± 0.01
1:1	0.21/0.25	0.75 ± 0.02	0.19 ± 0.02	12.6 ± 0.2	0.06 ± 0.01
2:1	0.27/0.17	0.63 ± 0.02	0.29 ± 0.02	14.0 ± 0.3	0.07 ± 0.02
3:1	0.31/0.13	0.59 ± 0.02	0.33 ± 0.02	14.3 ± 0.4	0.08 ± 0.02
D[c]	0.41/---	16.4 ± 0.5 ns	97 ± 4 ns		710 ± 10 ns
		0.56 ± 0.01	0.25 ± 0.01		0.19 ± 0.01

[a] Time constants are shared among the kinetics fitting of all mixing samples
[b] The donor-only sample is fit with different time constants.
[c] Amplitude-averaged.

Table S2. Fitting parameters for the acceptor kinetics of TCSPC data of coupled QDs with different D/A ratios.

D/A	OD_D/OD_A at 450 nm	τ_1, ns (amp.)[a] EnT	τ_2, ns (amp.)[a] EnT	τ_{EnT} (ave.)[b] ,ns	τ_3, ns Exciton decay
A	---/0.50	17.7 ± 0.7 (-0.39 ± 0.01)		17.7 ± 0.7	677 ± 1
1:2	0.14/0.33	10 ± 2 (-0.38 ± 0.07)	31 ± 4 (-0.37 ± 0.08)	15.0 ± 2.6	712 ± 1
1:1	0.21/0.25	9 ± 2 (-0.38 ± 0.06)	32 ± 2 (-0.68 ± 0.08)	16.7 ± 3.0	747 ± 1
2:1	0.27/0.17	11 ± 2 (-0.49 ± 0.07)	42 ± 2 (-0.96 ± 0.08)	21.5 ± 3.7	767 ± 2
3:1	0.31/0.13	16 ± 2 (-0.75 ± 0.08)	55 ± 3 (-1.06 ± 0.09)	27.4 ± 3.0	803 ± 2

[a] Negative amplitudes represent growths of PL signals.
[b] Averaged over amplitudes.

9. Rate Equation Model

In order to apply Förster theory to model the EnT dynamics, we firstly deconvoluted the ensemble of the DQDs (**Figure S15)** and AQDs (**Figure S16)** into three sub-populations by referring to the result of single-particle fluorescence measurements of PbS QDs[3].

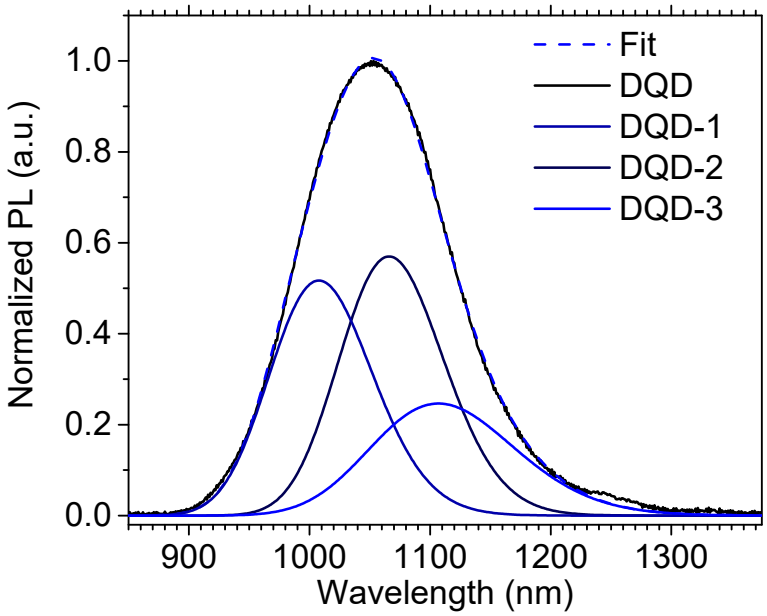

Figure S14. Deconvolution of ensemble DQD PL(black, solid) into 3 QD populations: DQD-1, DQD-2, and DQD-3. The sum of the 3 QD populations is plotted in the blue dashed line.

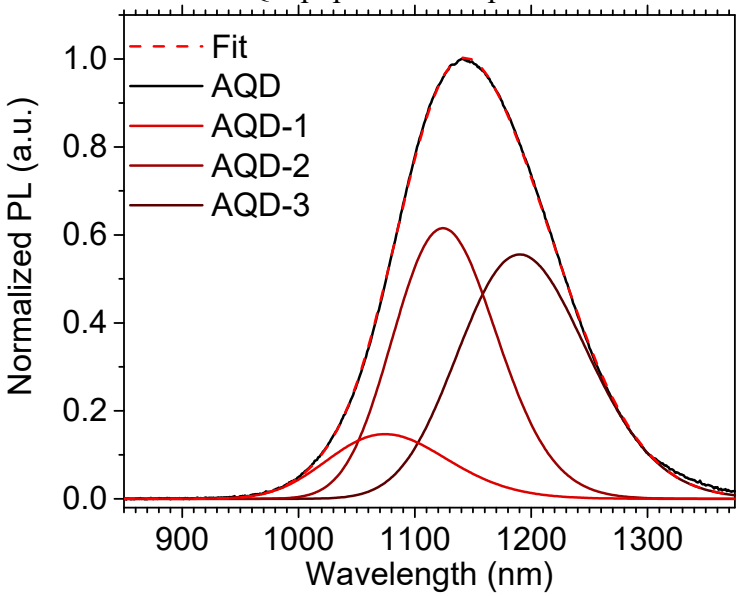

Figure S15. Deconvolution of ensemble AQD PL(black, solid) into 3 QD populations: AQD-1, AQD-2, and AQD-3. The sum of the 3 QD populations is plotted in the red dashed line.

We implemented an exciton hopping model similar to what has been previously used to describe FRET in metal-organic frameworks[4] and colloidal nanoplatelets[5], to model the energy transfer kinetics in our QD assemblies. The rate equation model (RE model) was governed by the master equation, eq S1, which allows for FRET between DQDs and AQDs as well as radiative/non-radiative relaxation of individual QDs:

$$\frac{d}{dt}P_i(t) = P_i(t)\left\{-\frac{1}{\tau_i} - \sum_{j\neq i} k_{i,j}\right\} + \sum_{j\neq i} k_{j,i}P_j(t) \qquad (S1)$$

where $P_i(t)$ represents the population of each QD subgroup, τ_i is the intrinsic relaxation lifetime of the QD excited state, and $k_{i,j}$ represents the rate of EnT from site *i* to site *j*. The model was implemented in Python 2.7 using the NumPy and SciPy libraries. First, we created 500 random-sized assemblies of QDs with the average size and standard deviation dictated by the TEM data (35 ± 8 nm). The structure of the QD assemblies was chosen to be hexagonally-close packed with the interparticle-spacing (4.8 ± 0.6 nm) and particle size determined by cryo-STEM. The average number of QDs in the simulation is 205± 31. We randomly assigned QDs to be either AQDs or DQDs based upon the experimental ratio of QD mixtures. We then further randomly assigned DQDs (AQDS) to each subgroup of DQDs (AQDs) based upon the results of spectral deconvolution shown in **Figures S15** and **S16**. For each QD assembly (composed of *n* QDs), we created an $n \times n$ matrix where element n_{ij} is the rate of FRET from QD *j* to QD *i*, and element n_{ii} is the rate of radiative/non-radiative relaxation of QD *i*. The rates of FRET between DQDs and AQDs were floating input parameters that served as the tunable parameters for fitting the TRPL kinetics with the model. To treat the non-radiative exciton decay which account for 77% for DQDs and 84% for AQDs according to their PL quantum yield, we arbitrarily assigned an ultrafast τ_i = 10 ps to these dark QDs which do not participate EnT. The lifetimes of emissive DQDs and AQDs were set as 710 ns and 680 ns, respectively, as measured by time-resolved PL. We arbitrarily initialized the system by exciting QDs within each assembly with an average excitation ratio of 5%. The relative probability of excited DQDs and AQDs were determined by their extinction coefficients at 450 nm (0.84:1 for DQD:AQD). We propagated the system in time using a Runge-Kutta algorithm and a 1 ps step size. 500 QD assemblies were averaged in fitting the kinetics of each coupled sample. The distance-dependence of EnT rate, was determined based on by Förster theory as **eq S2**:

$$\frac{1}{k_{j,i}} = \tau_R \left(\frac{R_{i,j}}{R_0}\right)^6 \qquad (S2)$$

where R_0 represents the Förster radius which was calculated using the EnT rate between nearest-neighbors ($k_{j,i}{}^{NN}$). Therefore, the only tunable fitting parameters in the global fitting were $k_{j,i}{}^{NN}$, and the results are listed in **Table S3**.

Table S3. Time Constants for Nearest-Neighbor FRET[a] between QD Subgroups Obtained from Globally Fitting PL Dynamics of Coupled QD Assemblies (**Figure S3**) to Eq 1.

	Donor Subgroup[b]				
Acceptor Subgroup[b]	DQD-1 τ_{EnT} (ns)	DQD-2	DQD-3	AQD-1	AQD-2
DQD-2	215 ±3 2	-	-	-	-
DQD-3	25 ± 4	200 ± 24	-	-	-
AQD-1	15 ± 5	52 ± 3	610 ± 70	-	-
AQD-2	53 ± 5	14 ± 3	380 ± 16	238 ± 18	-
AQD-3	68 ± 11	57 ± 4	14 ± 4	14 ± 3	54 ± 2

[a] These time constants correspond to FRET from one donor to one adjacent acceptor.

[b] Subgroups are divided based on deconvolution of the PL spectra of DQDs and AQDs.

We estimated the uncertainty of the fitting parameters by evaluating the coefficient of determination, R^2 for a range of modeling results. We stepwise vary the FRET lifetimes by 2.5 ns per step within the range of 2.5 ns to 2000 ns and calculated the R^2 value for each point. We then refined the FRET lifetime fitting at the local maximum of R^2 using a downhill simplex algorithm to determine the final FRET lifetimes listed in **Table S3**. We calculated the uncertainty in the final FRET parameters by iteratively changing the FRET lifetimes with 0.5 ns per step centered at the final FRET lifetimes and calculating the R^2 value for each point. The uncertainties listed in **Table S3** reflect the range of FRET lifetimes that yield an R^2 value > 0.95. We initially fit the DQD-only and AQD-only TR-PL kinetics to obtain the DQD-DQD and AQD-AQD FRET rates in order to reduce the codependency of the parameters. The DQD-DQD and AQD-AQD FRET rates were then used as input parameters to globally fit the DQD-AQD FRET rates using the mixed ratio TR-PL kinetics.

We also implemented a kinetic Monte Carlo (KMC) model – which, in principle, better represents the exciton dynamics in randomly mixed donor-acceptor assemblies – for the DQD:AQD = 1:1 data to double check the simulation results of RE model. We used the same parameters described earlier for the RE model and performed ten million trajectories for 500 QD assemblies. The KMC model yielded a very similar result to the RE model, as shown in **Figure**

A

S17. Given the KMC model is computationally much more expensive, we decided to only use RE model to simulate all the kinetic data.

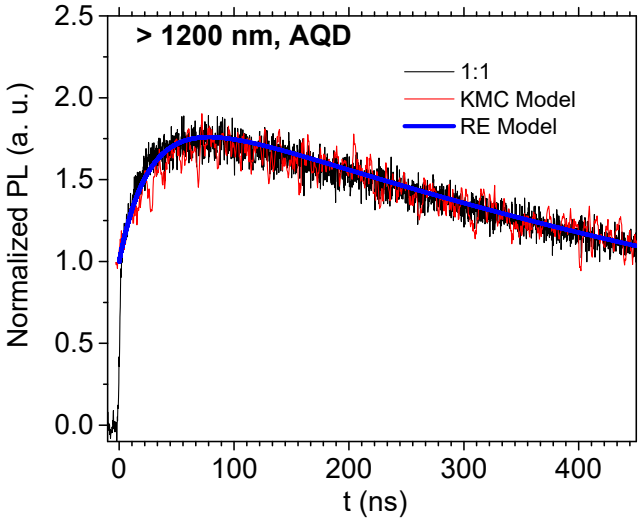

Figure S17. Comparison of the kinetic fitting for DQD/AQD = 1:1 mixture using the RE model (blue) and KMC model (red).

We calculated the diffusivity of excitons by fitting the population at each QD for the rate equation model to **eq S3:**[4]

$$P(r,t) = \frac{1}{4\pi Dt} e^{-\frac{r^2}{4Dt}} \qquad (S3)$$

where P(r,t) represents the population at distance, r, and time t, and D is the exciton diffusivity. In contrast to the earlier modeling for rate constants, we excited only one quantum dot per cluster, and this initial exciton was placed in the center of the QD assemblies. All other parameters, including thee QD assembly size, interparticle-distance and FRET rates (**Table S3**) were kept the same as the previous modeling. We fit the diffusion for the full set of distances spanning the size of the QD assemblies and a suitable range of times. The results were used to calculate the mean diffusion lengths and exciton hopping steps, as listed in **Table S4**.

Table S4. Exciton Diffusion Parameters Obtained by Rate Equation Model.

Samples	DQD-only	AQD-only	DQD:AQD Ratio			
			1:2	1:1	2:1	3:1
D ($\times 10^{-7}$ cm^2/s)	4.4	4.7	7.3	9.2	13.3	15.5
L (nm)	5.5	5.8	7.2	8.1	9.7	10.5
n_{hops}	1.1	1.2	1.5	1.7	2.0	2.2

9. Cryo-STEM Images of Coupled and Uncoupled Samples of a DQD-AQD Mixture.

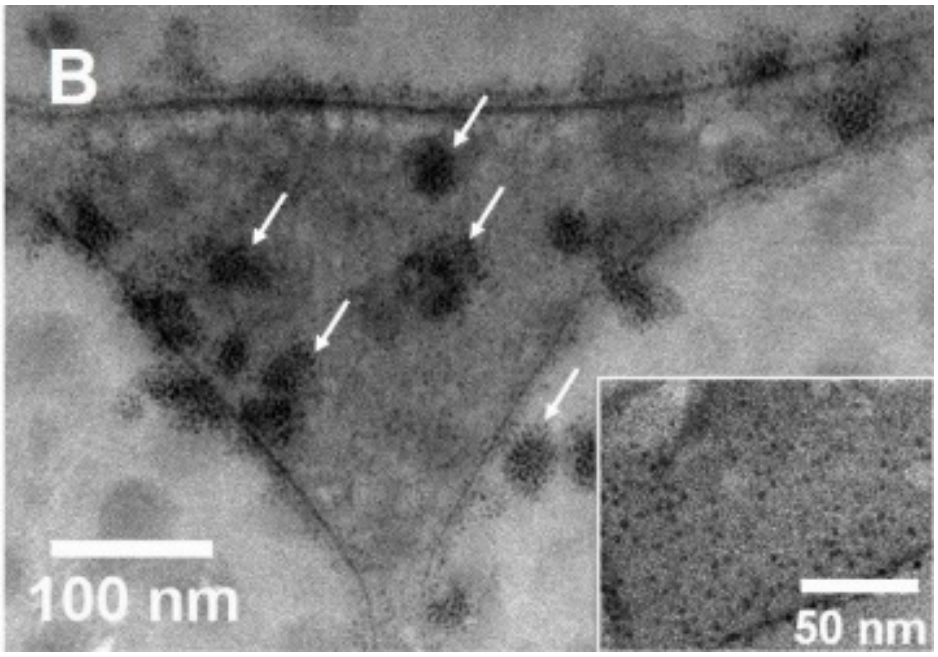

Figure S18. Cryo-STEM image of assembled PbS QDs with DQD:AQD = 3:1, upon addition of 30 eq. of Zn^{2+} per QD (also Figure 1B in the main text). *Inset*: uncoupled QD sample with the same DQD:AQD ratio.

References

1. Hines, M. A.; Scholes, G. D. *Adv. Mater.* **2003**, *15*, 1844.
2. Xu, F.; Ma, X.; Haughn, C. R.; Benavides, J.; Doty, M. F.; Cloutier, S. G. *ACS Nano* **2011**, *5*, 9950.
3. Valiev, M.; Bylaska, E. J.; Govind, N.; Kowalski, K.; Straatsma, T. P.; Van Dam, H. J. J.; Wang, D.; Nieplocha, J.; Apra, E.; Windus, T. L.; de Jong, W. A. *Computer Phys. Commun.* **2010**, *181*, 1477.
4. Peterson, J. J.; Krauss, T. D. *Nano Lett.* **2006**, *6*, 510.
5. Zhang, Q.; Zhang, C.; Cao, L.; Wang, Z.; An, B.; Lin, Z.; Huang, R.; Zhang, Z.; Wang, C.; Lin, W. *J. Am. Chem. Soc.* **2016**, 138, 5308.
6. Guzelturk, B.; Erdem, O.; Olutas, M.; Kelestemur, Y.; Demir, H. V. *ACS Nano* **2014**, *8*, 12524.